SOLAR CELLS

Aqueous synthesis of perovskite precursors for highly efficient perovskite solar cells

Peide Zhu[1,2]†, Deng Wang[1,2,3]†, Yong Zhang[1,2]*†, Zheng Liang[4], Jingbai Li[5], Jie Zeng[1,2,3], Jiyao Zhang[1,2], Yintai Xu[1], Siying Wu[6], Zhixin Liu[1,2], Xianyong Zhou[1,2], Bihua Hu[1,2], Feng He[7], Lin Zhang[8], Xu Pan[4], Xingzhu Wang[1,9,10]*, Nam-Gyu Park[11,12]*, Baomin Xu[1,2]*

High-purity precursor materials are vital for high-efficiency perovskite solar cells (PSCs) to reduce defect density caused by impurities in perovskite. In this study, we present aqueous synthesized perovskite microcrystals as precursor materials for PSCs. Our approach enables kilogram-scale mass production and synthesizes formamidinium lead iodide ($FAPbI_3$) microcrystals with up to 99.996% purity, with an average value of 99.994 ± 0.0015%, from inexpensive, low-purity raw materials. The reduction in calcium ions, which made up the largest impurity in the aqueous solution, led to the greatest reduction in carrier trap states, and its deliberate introduction was shown to decrease device performance. With these purified precursors, we achieved a power conversion efficiency (PCE) of 25.6% (25.3% certified) in inverted PSCs and retained 94% of the initial PCE after 1000 hours of continuous simulated solar illumination at 50°C.

Although perovskite solar cells (PSCs) offer the potential for low-cost fabrication and high power conversion efficiency (PCE) of 26.1% (*1*), defects in the perovskite layer have been a major challenge to achieve high PCEs (*2*, *3*), and previous studies have primarily focused on passivating these defects through additives (*4*–*6*) or interfacial modifications (*7*–*9*). In addition to defect passivation, impurities in commercial lead iodide (PbI_2) reagents can catalyze perovskite solution degradation and the formation of harmful by-products (*10*). Moreover, a nonstoichiometric ratio of formamidinium iodide (FAI) and PbI_2 in the precursor mixture can cause I_2 impurity generation and lower the solution's pH with aging, which ultimately reduces PSC performance (*11*, *12*). Precursor quality plays a crucial role in addressing these challenges, with high-purity precursor materials demonstrating considerable potential in minimizing the impurity-induced intrinsic defects (*13*–*16*). Thus, finding ways to remove precursor impurities, along with a better understanding of the effects of impurities, could improve PSCs performance.

One approach to address these intrinsic factors is to use crystallization for purification; in this case, redissolving presynthesized perovskite microcrystal powders as precursors for subsequent perovskite film fabrication. This method can achieve a high degree of crystal orientation, accurate stoichiometric ratio, and low trap-state density (*17*, *18*). Notably, perovskite microcrystals such as methylammonium lead iodide ($MAPbI_3$) and formamidinium lead iodide ($FAPbI_3$) have been used as precursors for PSCs fabrication (*17*, *19*). The mainstream methods for synthesizing these perovskite crystals rely on mechanochemistry or wet chemistry with organic solvents such as acetonitrile (ACN) (*20*–*22*), 1,4-butyrolactone (*23*), and 2-methoxyethanol (2-ME) (*19*, *24*). Nevertheless, these approaches are plagued by challenges related to achieving high purity, minimizing environmental impact, and optimizing yields. Moreover, there is a notable absence of studies that quantitatively assess the purity of synthesized perovskite microcrystals.

The use of water as a solvent for perovskite synthesis could take advantage of its polarity, hydrogen bonding capabilities, its low volatility at room temperature, and is more environmentally suitable. However, the current use of water as a solvent in the synthesis of perovskite microcrystals remains relatively constrained. Therefore, there is a need to develop an aqueous solvent that can be scaled up for the synthesis of high-purity crystals and improve the quality of perovskite films.

In this work, we present the synthesis and characterization of an aqueous-synthesized perovskite microcrystal (ASPM) that enhanced the quality of perovskite precursors. The high yield of 92% was obtained in a kilogram-scale synthesis of $FAPbI_3$, with a materials cost two orders of magnitude lower than that of commercial PbI_2 and FAI. By removing the impurities of calcium (Ca^{2+}), which has the highest impurity concentration, along with the sodium (Na^+) and potassium (K^+) ions in the aqueous solution, the purity of $FAPbI_3$ microcrystals achieved an average value of 99.994 ± 0.0015%. Removal of these ions led to a reduced defect density and extension of carrier diffusion length within the resultant perovskite film, which contributed to the superior performance of PSCs.

Aqueous synthesis of perovskite microcrystals

We first investigated the properties of the solvents used for synthesizing high-quality perovskite microcrystals to find out the selection criteria. We compared the solubility of δ-$FAPbI_3$ in aqueous solvents and other commonly used solvents in PSCs (Fig. 1A). The relations between Gutmann donor number (D_N), dielectric constant (ε_r), and median lethal dose (LD_{50}) for the solvents were shown in Fig. 1B and table S1. Solvents with low D_N and ε_r, indicated in gray, such as ethyl ether (Et_2O) and ethyl acetate (EA), did not dissolve perovskite and are ideal antisolvents for film synthesis. Conversely, solvents with a D_N exceeding 20 kcal/mol exhibited excellent solubility for $FAPbI_3$ microcrystals, including *N*,*N*-dimethylformamide (DMF) and dimethyl sulfoxide (DMSO) (indicated in orange), as they could strongly coordinate with Pb^{2+} in $FAPbI_3$. Solvents with $\varepsilon_r > 18$ but $D_N < 20$ kcal/mol, such as ethanol (EtOH), isopropanol (IPA), and water (H_2O), dissolved the FAI in $FAPbI_3$ without dissolving PbI_2. Notably, H_2O has a much larger LD_{50} value compared with that of the other solvents and could dissolve PbI_2 in the presence of I^- ion. The stability of $FAPbI_3$ in H_2O could be adjusted by adding hydrogen iodide (HI) (47 wt.%). As shown in Fig. 1A, $FAPbI_3$ was nearly insoluble at a certain concentration of HI, which may have been because the I^- in the HI solution can stabilize the $FAPbI_3$ octahedral framework (*25*), indicating the possibility of $FAPbI_3$ synthesis in aqueous solution.

To confirm the feasibility of synthesizing $FAPbI_3$ in aqueous solution, we studied the HI concentration–dependent solubility of FAI, PbI_2, and $FAPbI_3$ (Fig. 1C). In a 2-mol/L HI solution, FAI exhibited a high solubility of >5 mol/100 g, whereas PbI_2 had a low solubility of $<1 \times 10^{-2}$ mol/100 g. $FAPbI_3$ decomposed

[1]Department of Materials Science and Engineering and Shenzhen Engineering Research and Development Center for Flexible Solar Cells, Southern University of Science and Technology, Shenzhen 518055, China. [2]Key University Laboratory of Highly Efficient Utilization of Solar Energy and Sustainable Development of Guangdong, Southern University of Science and Technology, Shenzhen 518055, China. [3]Department of Materials Science and Engineering, City University of Hong Kong, Kowloon 999077, Hong Kong. [4]Key Laboratory of Photovoltaic and Energy Conservation Material, Institute of Solid-State Physics, Hefei Institutes of Physical Science (HIPS), Chinese Academy of Sciences, Hefei 230031, China. [5]Hoffmann Institute of Advanced Materials, Shenzhen Polytechnic University, Shenzhen 518055, China. [6]Department of Biomedical Engineering, Southern University of Science and Technology, Shenzhen 518055, China. [7]State Key Laboratory on Tunable Laser Technology, School of Electronic and Information Engineering, Harbin Institute of Technology, Shenzhen 518055, China. [8]Hunan Key Laboratory for Super Microstructure and Ultrafast Process, School of Physics, Central South University, Changsha 410083, China. [9]Academy for Advanced Interdisciplinary Studies, Southern University of Science and Technology, Shenzhen 518055, China. [10]Shenzhen Putai Technology Co., Ltd, Shenzhen 518110, China. [11]School of Chemical Engineering and Center for Antibonding Regulated Crystals, Sungkyunkwan University (SKKU), Suwon 16419, Republic of Korea. [12]SKKU Institute of Energy Science & Technology (SIEST), Sungkyunkwan University, Suwon 16419, Republic of Korea.
***Corresponding author. Email: zhangy8@sustech.edu.cn (Y.Z.); wangxz@sustech.edu.cn (X.W.); npark@skku.edu (N.-G.P.); xubm@sustech.edu.cn (B.X.)**
†These authors contributed equally.

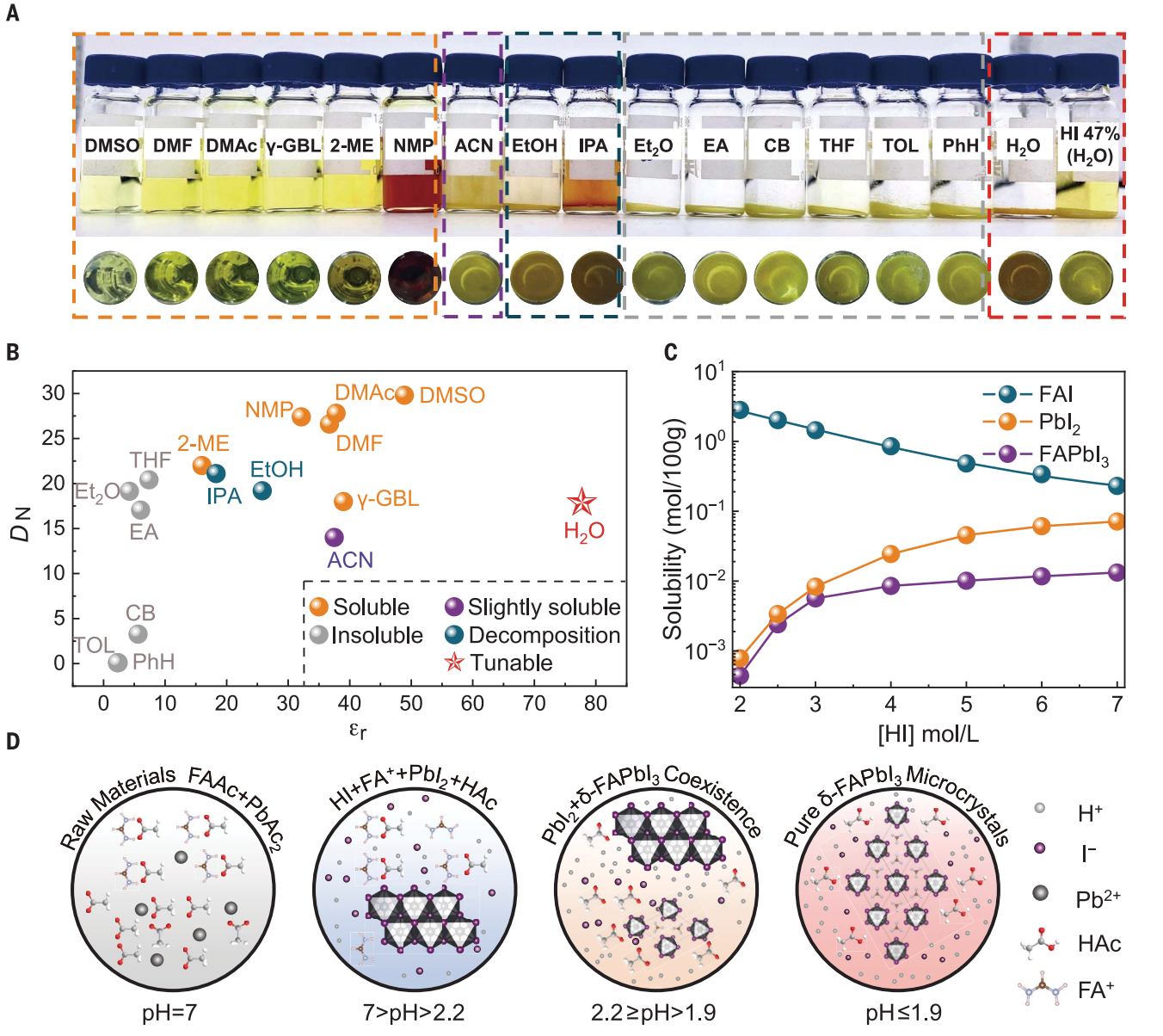

Fig. 1. Aqueous synthesis of $FAPbI_3$ perovskite microcrystals. (**A**) Front and bottom photographs of the 1-mL various solvent vials containing 1 mmol of δ-$FAPbI_3$ at room temperature. The dashed boxes represent the corresponding colored solubility (B). γ-GBL, γ-butyrolactone; PhH, benzene; TOL, toluene; CB, chlorobenzene; DMAc, dimethylacetamide; NMP, N-methyl-2-pyrrolidone. (**B**) D_N and ε_r of the various solvents. (**C**) HI concentration–dependent solubility of FAI, PbI_2, and $FAPbI_3$. (**D**) Schematic illustration of $PbAc_2$ and FAAc in different pHs of HI aqueous solution.

into PbI_2 and FAI, with PbI_2 precipitating and FAI dissolving. As the concentration of HI increased, the solubility of PbI_2 increased to over 1×10^{-1} mol/100 g, whereas the solubility of FAI showed a slight decrease but remained high. By contrast, $FAPbI_3$ showed negligible solubility compared with PbI_2. These results indicate the potential for synthesizing $FAPbI_3$ perovskite microcrystals from FAI and PbI_2 in an HI aqueous solution.

Considering the sources of FAI and PbI_2, we synthesized the $FAPbI_3$ perovskite microcrystals using aqueous-soluble lead acetate trihydrate ($PbAc_2{\cdot}3H_2O$, 99.5% purity) and formamidine acetate (FAAc, 99% purity) as raw materials in HI aqueous solution. We confirmed the potential elemental impurities through an inductively coupled plasma-optical emission spectrometer (ICP-OES), which is a semiquantitative elemental full-spectrum scanning analysis test. Impurity analysis revealed the presence of inorganic metal elements (Ca, Na, and K) in the raw materials (table S2), which are also found in conventional precursors [cesium iodide (CsI), methylammonium iodide (MAI), FAI, and even 99.99%-purity PbI_2] (fig. S1 and table S3).

The synthesis solution's pH played a crucial role in by-product formation (Fig. 1D and fig. S2). At pH = 7, the aqueous solution of $PbAc_2$ and FAAc (1:1) remained in the solution without any precipitate (Eqs. 1 and 2). For 7 > pH > 2.2, $PbAc_2$ reacted with HI to form weak acetic acid (HAc) (Eq. 3), and PbI_2 began to precipitate (Eq. 4). If the reactant content was low, $FAPbI_3$ could not form as it dissolved. By keeping pH between 1.9 and 2.2, PbI_2 dissolved and converted into $PbI_{(2+x)}^{x-}$ scaffolds (*26*). In this regime, the reaction in Eq. 5 dominated the system. When the pH was <1.9, the solubility of PbI_2 products remained high, and the intercalation of FA^+ into the $PbI_{(2+x)}^{x-}$ scaffolds led to the formation of $FAPbI_3$ (Eq. 6) without observing the PbI_2 peak signal in the x-ray diffraction (XRD) pattern (fig. S2). Therefore, we used an optimized pH below 1.9 and an optimized $PbAc_2$:

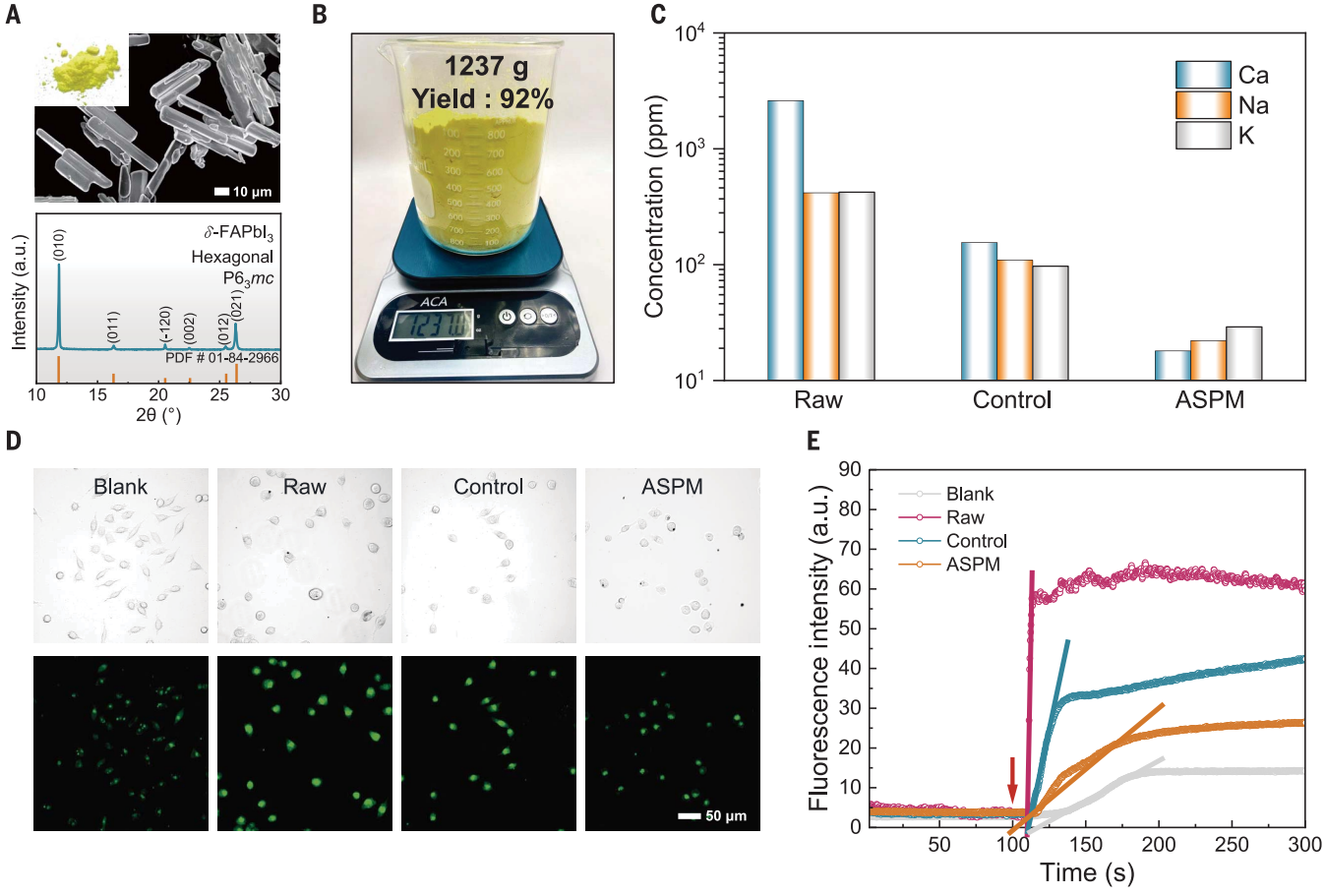

Fig. 2. The purification of aqueous synthesized perovskite microcrystals. (**A**) SEM images (top) and XRD pattern (bottom) of δ-$FAPbI_3$ microcrystals. a.u., arbitrary units. (**B**) Digital photograph of large-scale synthesized δ-$FAPbI_3$ microcrystals. (**C**) ICP-OES results of major elements. Raw, control, and ASPM are respectively present for 1:1 $PbAc_2$:FAAc, 1:1 PbI_2:FAI, and aqueous synthesized δ-$FAPbI_3$ microcrystals. (**D**) Qualitative comparison of Ca^{2+} ion content in raw materials and synthesized perovskite microcrystals by means of Ca^{2+} ion fluorescent probe technology. The optical images (top) and confocal fluorescence images (bottom) of the L929 fibroblasts loaded with Fluo-4 AM after ionomycin stimulation. Blank is original cells without any added test sample. (**E**) Time-dependent change of the fluorescence in a Fluo-4 AM–loaded L929 fibroblasts in response to ionomycin. The arrow indicates the time at which ionomycin was added.

FAAc:HI molar ratio of 1:1.2:3.2 for high-quality $FAPbI_3$ perovskite microcrystals with minimal by-products (fig. S3).

$$PbAc_2 \rightarrow Pb^{2+} + Ac^- \quad (1)$$

$$FAAc \rightarrow FA^+ + Ac^- \quad (2)$$

$$H^+ + Ac^- \rightarrow HAc \quad (3)$$

$$Pb^{2+} + I^- \rightarrow PbI_2\downarrow \quad (4)$$

$$PbI_2 + xI^- \rightarrow PbI_{(2+x)}^{x-} \quad (5)$$

$$PbI_{(2+x)}^{x-} + FA^+ \rightarrow FAPbI_3\downarrow \quad (6)$$

We used scanning electron microscopy (SEM) and XRD to analyze the morphology and structure of the resulting $FAPbI_3$ perovskite microcrystal. The synthesized yellow powder displayed a one-dimensional (1D) rod-type shape with a maximum length of 50 μm and exhibited a typical hexagonal δ phase with $P6_3mc$ space group (Fig. 2A) (*27*). Energy dispersive spectroscopy (EDS) for the chemical composition mapping of one δ-$FAPbI_3$ microcrystal showed the uniform distribution of the N, Pb, and I elements in the crystal (fig. S4). A high yield of $FAPbI_3$ microcrystals (92%, 1237 g) was obtained in a single batch (Fig. 2B), demonstrating the potential for large-scale commercialization of PSC precursors. Notably, this synthesis method allows for the synthesis of other 3D perovskites (fig. S5). We denoted these aqueous synthesized perovskite microcrystals as ASPM.

To comprehensively analyze impurities in the raw materials $PbAc_2$+FAAc (denoted as "raw"), conventional precursor PbI_2+FAI (denoted as "control"), and ASPM, we conducted quantitative element analysis using ICP-OES, considering a total of 62 metal impurities. As shown in Fig. 2C, Ca^{2+}, Na^+ and K^+ were the predominant impurities in the raw materials, with a total impurity concentration >3500 parts per million (ppm), and the control sample also exhibited an impurity concentration of ~380 ppm (table S4). However, the aqueous synthesized $FAPbI_3$ reduced the impurity concentration to <80 ppm (table S5). This substantial reduction in impurity content compared with that of the raw and control powders indicated that the purification process was effective.

We conducted a Ca^{2+} fluorescence probe experiment on the powders to visually demonstrate the impurity of Ca^{2+} ion (*28*). Fluo-4 AM, a cell-permeable acetoxymethyl ester, has enhanced fluorescence intensity upon binding Ca^{2+} (*29*). In Fig. 2D, the green fluorescence of the raw and control powders was brighter than that of the ASPM powder. The ASPM powder also showed the gentlest rise slope of 0.307 (table S6), with the lowest final intensity except for the blank sample, reflecting the exceptionally low concentration of Ca^{2+} in ASPM (Fig. 2E). We

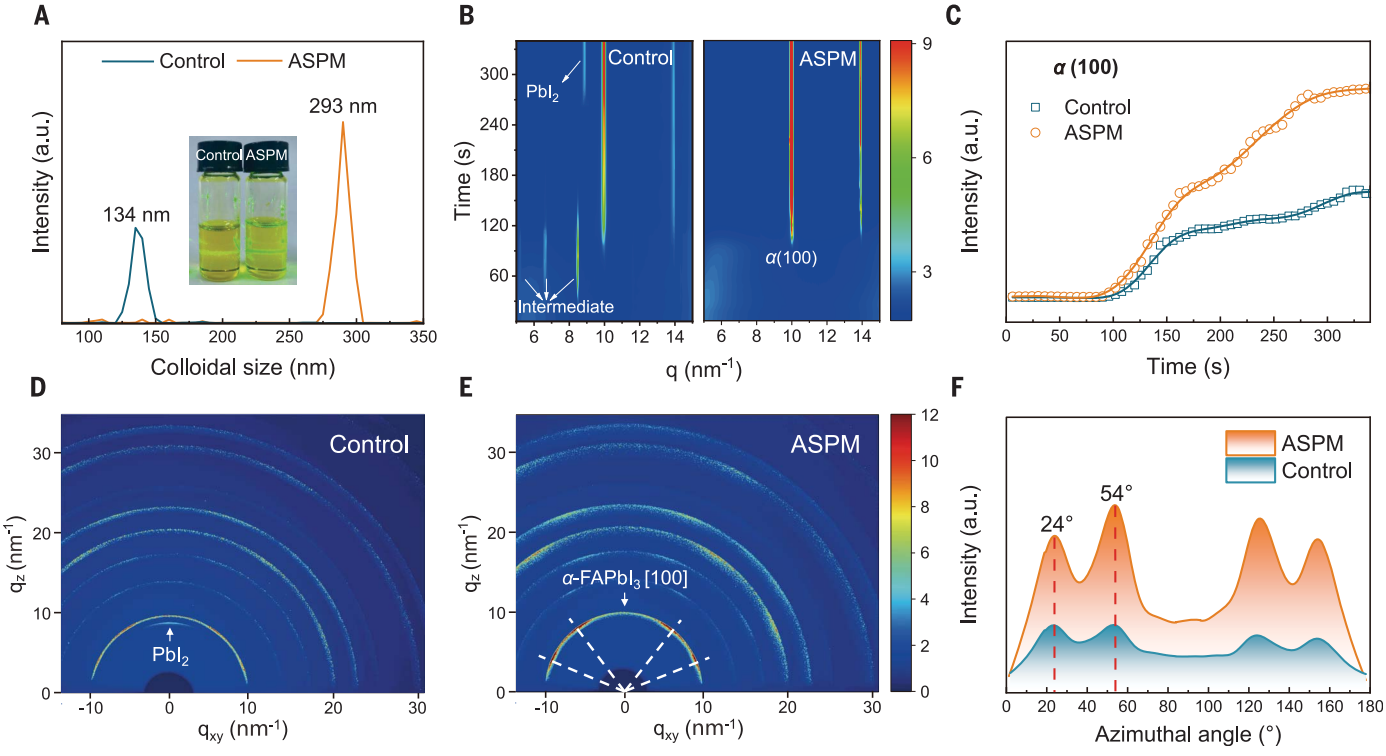

Fig. 3. The nucleation and crystallization process of perovskite films. (**A**) DLS of the $FA_{0.85}MA_{0.1}Cs_{0.05}PbI_3$ prepared from the conventional mixture (denoted as control) precursor and perovskite microcrystals (denoted as ASPM) precursor. (**B**) In situ GIWAXS measurements of the as-coated perovskite solution from the control and ASPM precursors under 100°C annealing. *q*, scatter vector. (**C**) The integrated intensity of α (100) peak versus annealing time extracted from the in situ GIWAXS results. (**D** and **E**) 2D GIWAXS images of perovskite films from control (D) and ASPM (E) precursors deposited on a silicon wafer substrate. The incidence angle is 1°. q_z, out-of-plane scattering vector; q_{xy}, in-plane scattering vector. (**F**) The integrated intensity plots azimuthally along the ring assigned to the α-$FAPbI_3$ (100) lattice plane.

attributed the reduction of impurity ions to the extensive dissolution of these ionic salts by the aqueous solution in the reaction. As shown in fig. S6A, the solubility of the CaI_2 was >230 g in 100 g of H_2O, which was two orders of magnitude higher than in organic solvents such as ACN (6.99 g/100 g) and 2-ME (4.69 g/100 g). Thus, the concentration of Ca^{2+} (as well as that of Na^+ and K^+) in $FAPbI_3$ microcrystals synthesized from aqueous solution were lower compared with those synthesized from ACN and 2-ME (fig. S6B). The $FAPbI_3$ perovskite synthesized in aqueous solution exhibited a champion purity of 99.996% with an average value of 99.994 ± 0.0015%, surpassing that of those synthesized in organic solvents (99.831% in ACN and 99.815% in 2-ME) (fig. S6C). Additionally, we confirmed the absence of noticeable hydrogen-containing impurities in $FAPbI_3$ microcrystals through the ^1H nuclear magnetic resonance (NMR) spectrum (fig. S7). Furthermore, we ascertained the exceptional dryness of the synthesized microcrystals with a trace water content of 101.0 ± 15.0 ppm (table S7).

We calculated the materials cost of the aqueous synthesized δ-$FAPbI_3$ microcrystals for kilogram-scale synthesis. The materials cost of δ-$FAPbI_3$ microcrystals was as low as US$0.2259 per gram, which was nearly two orders of magnitude lower than the retail prices of commercial PbI_2 and FAI (tables S8 and S9). The δ-$FAPbI_3$ microcrystals also showed six-month storage stability under ambient conditions (fig. S8). The thermogravimetric analysis (TGA) and differential thermal analysis (DTA) indicated a precise stoichiometric ratio of $FAPbI_3$ (figs. S9 and S10).

Perovskite film crystallization

To prepare a precursor solution for the fabrication of $FA_{0.85}MA_{0.1}Cs_{0.05}PbI_3$ perovskite film, we used a mixture of aqueous synthesized $FAPbI_3$, $MAPbI_3$, and $CsPbI_3$ microcrystals and the mixture of commercial FAI, PbI_2, CsI, and MAI in solvents for the ASPM and control precursor solution, respectively. As shown in the dynamic light scattering (DLS) measurement (Fig. 3A), the control precursor formed colloids with an average size of 134 nm, whereas the ASPM precursor contained larger colloids with an average size of 293 nm. The ASPM displayed a stronger typical Tyndall effect that also confirmed the presence of larger colloids.

We used synchrotron-based in-situ grazing-incidence wide-angle x-ray scattering (GIWAXS) to analyze the crystallization kinetics of the as-coated perovskite solution under annealing for 340 s. As shown in Fig. 3B, at the initial state, three peaks were found in control films located at scattering vector q = 5.21, 6.64, and 8.49 nm^{-1}, which were assigned to the perovskite intermediate phase of DMSO adduct or the hexagonal perovskite polytype 2H (*30*). However, in the ASPM film, no obvious peak was observed at the initial state given the presence of the amorphous perovskite colloids.

As the annealing time increased, the α-phase $FAPbI_3$ (100) plane of both two films appeared at the same time. The control perovskite film phase formed from the intermediate phase, whereas the ASPM perovskite film formed directly from the $FAPbI_3$ colloids. During annealing for ~250 s until the formation of the final state, the PbI_2 peak appeared in the control perovskite film, indicating the occurrence of nonstoichiometric or unbalanced composition reactions in the perovskite film for the control precursor solution. However, the PbI_2 peak was absent in the ASPM perovskite film because of the stoichiometric composition. For the ASPM film, the peak of α-$FAPbI_3$ (100) became more intense, indicating the generation of high-quality α-$FAPbI_3$ films (Fig. 3C). The SEM and AFM results showed that the surface morphology of the film fabricated from the ASPM precursor was compact and flat, whereas the one derived from the control precursor exhibited wider grain boundaries with some small crystals filled (fig. S11).

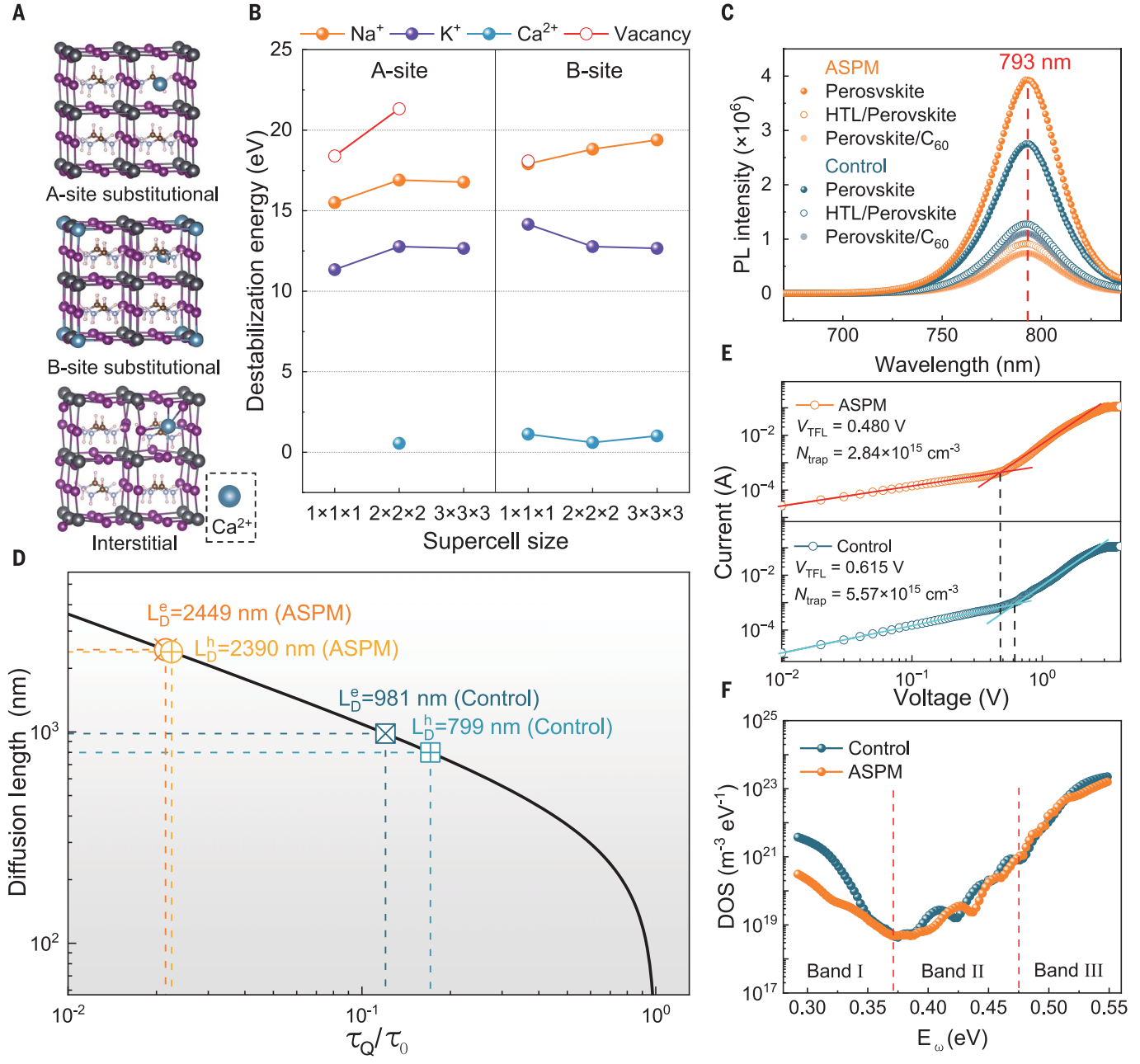

Fig. 4. Carrier transport mechanism. (**A**) Representative DFT calculation of Ca^{2+} in α-$FAPbI_3$ lattices using 2×2×2 perovskite supercells. (**B**) The calculated destabilization energy of the three defect models (FA^+ site substitution, Pb^{2+} site substitution, and interstitial) based on the 1×1×1, 2×2×2, and 3×3×3 perovskite supercell size. The absence of certain data means the results are unavailable because the cells were distorted and not converged correctly during the geometry optimization, which suggests highly unstable defects. (**C**) Steady-state PL spectra of the control and ASPM precursor–based perovskite films, HTL/perovskite films, and perovskite/C_{60} films. (**D**) The charge-carrier diffusion length of the control and ASPM precursor–based perovskite films. (**E**) Dark current (*I*)–voltage (*V*) data for hole-only devices based on control and ASPM precursors. V_{TFL}, trap filled limit voltage. (**F**) tDOS obtained by thermal admittance spectroscopy for the control and ASPM devices.

The 2D GIWAXS patterns shown in Fig. 3, D and E, exhibited an intense and integrated Debye-Scherrer ring at $q = 10\ nm^{-1}$, which corresponded to the α-$FAPbI_3$ (100) lattice plane. To obtain azimuthal-dependent intensities, we extract 1D integrated intensity data for the α-$FAPbI_3$ (100) plane in GIWAXS patterns (Fig. 3F). The preferred azimuthal angles 24° (156°) and 54° (126°) of ASPM film confirmed that the large-sized polyiodide colloids could trigger the preferred orientation during film formation (fig. S12), in which two dominant preferred orientations could improve carrier transport compared with random distributions and reduced shallow traps (*31*).

Charge transport

To find out how the presence of impurities affected the stability of the perovskite structure, we used density-functional theory (DFT) to calculate the destabilization energies associated with the placement of impurities, including Ca^{2+}, Na^+, K^+, and vacancies, within the $FAPbI_3$ perovskite lattice. The DFT was conducted by using three different models (A-site substitution, B-site substitution, and interstitial site) and varying perovskite supercell sizes (1×1×1, 2×2×2, and 3×3×3 perovskite supercells) (Fig. 4A, fig. S13, and table S10). The destabilization energy was the unstable energy for the defect states

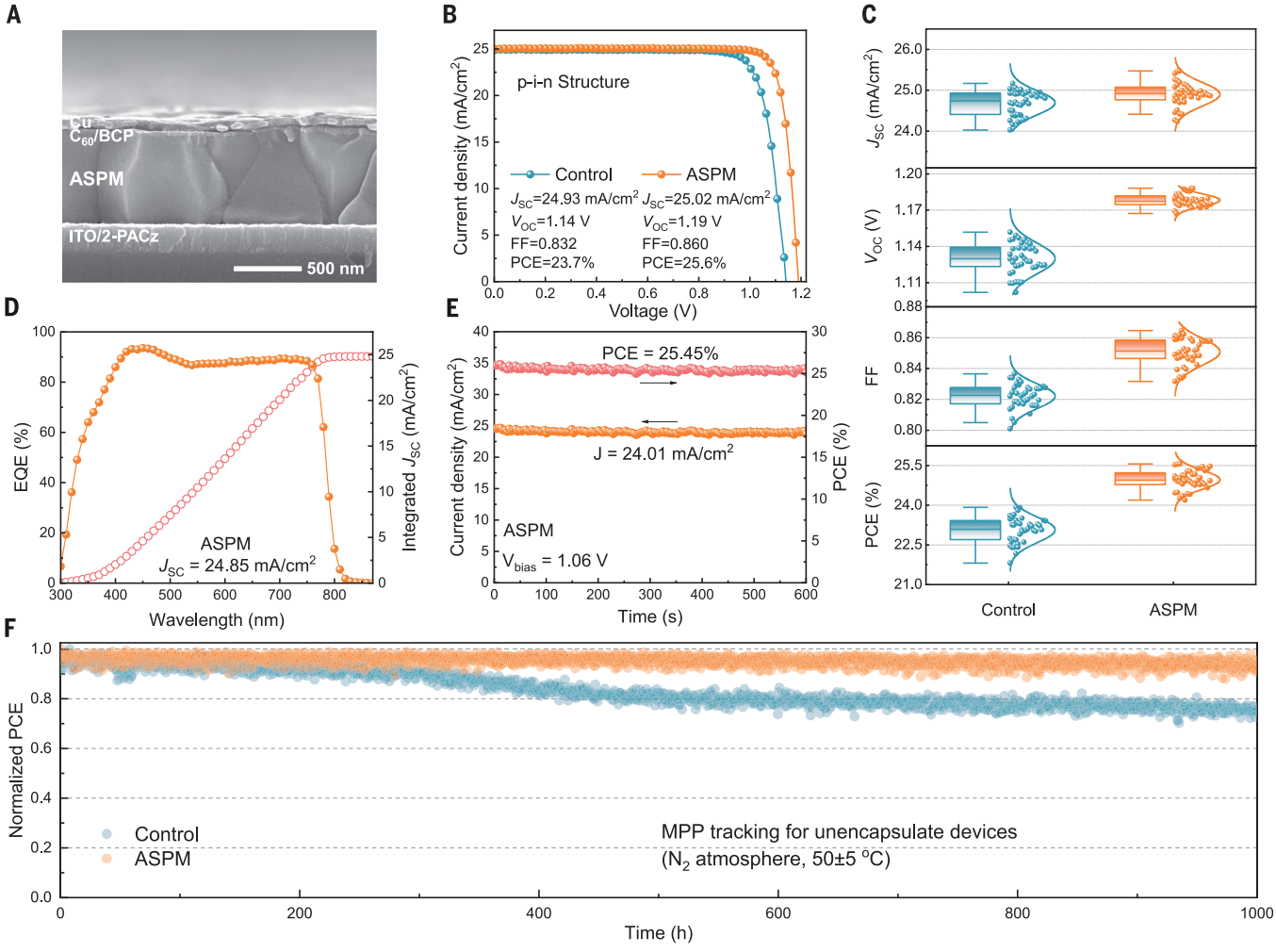

Fig. 5. Characterization of the PSCs. (**A**) Cross-sectional SEM image of the p-i-n PSCs. (**B**) Current density–voltage (*J-V*) curves of control and ASPM precursor-based PSCs. (**C**) Statistics of the photovoltaic parameters of PSCs based on control and ASPM precursors. (**D**) EQE spectra and integrated J_{SC} of the champion ASPM precursor–based PSCs. (**E**) The stabilized output of the champion device tracked at the MPP under standard AM 1.5G illumination. (**F**) Unencapsulated PSC performance tracking at the MPP under continuous AM 1.5G illumination for 1000 hours in N_2 atmosphere.

compared with that of the pure perovskite (0 eV) by the introduction of ions or vacancy, suggesting that the existence of defects contributes to the instability of the perovskite structure. As shown in Fig. 4B, the destabilization energy for Ca^{2+}, Na^+, K^+, and vacancy was Ca^{2+} < K^+ < Na^+ < vacancy, regardless of the supercell size. We constructed various supercells with substitution ratios of 20, 2.5, and 0.7%. Nevertheless, the observed changes in the instability energy were negligible for this range of supercells, implying that even a small quantity of impurity can destabilize the perovskite structure and affect the charge-carrier transport.

We conducted additional DFT calculations to evaluate the defect band energy associated with both Ca-introduced defects and intrinsic defects, alongside their defect formation energy within the context of three distinct I conditions for $FAPbI_3$ film growth, as shown in figs. S14 and S15 and table S11. The results reveal that Ca^{2+} could serve as shallow traps in the $FAPbI_3$, underscoring the necessity of eliminating Ca^{2+} in the perovskite.

We observed the photogenerated carrier behavior of the perovskite film through the photoluminescence (PL) and time-resolved photoluminescence (TRPL) spectra. The PL spectra at 793 nm showed no peak shift between control and ASPM films, indicating similar optical bandgaps (Fig. 4C and fig. S16). The steady-state PL intensity of the ASPM film showed higher intensity than that of the control film, which was attributed to the lower concentration of impurities. TRPL was measured on the control and ASPM perovskite films with or without a carrier quenching layer (fig. S17). TRPL data demonstrated approximately two times longer average carrier lifetimes (τ_{ave}) for the ASPM perovskite film compared with that of the control film (3163 ns versus 1675 ns) (table S12) (*32*). By conducting the temperature-dependent PL and TRPL (figs. S18 and S19 and table S13) as complementary analyses, we can reasonably infer that the shorter average carrier lifetimes may be attributed to the presence of quenching traps in the control perovskite films.

We evaluated the charge-carrier diffusion length on the basis of the TRPL results of perovskite films with a carrier quenching layer {[2-(9*H*-carbazol-9-yl) ethyl] phosphonic acid (2-PACz) and C_{60} for hole and electron quenching, respectively} according to a simplified 1D diffusion model (Eq. 7) (*33*):

$$\frac{L_D}{L} = \frac{2}{\pi}\sqrt{\frac{1}{\tau_Q/\tau_0} - 1} \quad (7)$$

where L_D is the charge-carrier diffusion length, L is the thickness of the perovskite film, and τ_Q

and τ_0 are the time-resolved photoluminescence with or without the quenching layer, respectively. The result showed that the electron and hole diffusion lengths of control films were 981 and 799 nm, respectively, whereas ASPM showed electron and hole diffusion lengths of 2449 and 2390 nm, respectively, indicating a prolonged charge-carrier lifetime and balanced charge extraction (Fig. 4D). The ASPM films also displayed a lower density of trap states within the bandgap (figs. S20 and S21 and table S14).

We estimated the trap densities (N_{trap}) using the hole-only device structure of glass/ITO/2-PACz/perovskite/Au. The N_{trap} of the ASPM film was calculated to be 2.84×10^{15} cm^{-3}, which was lower than that of the control device (5.57×10^{15} cm^{-3}) (Fig. 4E, fig. S23, and table S15). We also conducted temperature-dependent thermal admittance spectroscopy to distinguish the trap states in PSCs. The shallow trap states were more likely to originate internally within the perovskite (Band I), whereas the deep trap states primarily correlated with surface defects in the perovskite (Bands II and III) (*34*). In the ASPM, the trap density of states (tDOS) intensity decreased 10-fold in the Band I region (Fig. 4F, figs. S22 and S23, and table S16). The Band I region could be related to the impurities present in the perovskite films, particularly the Ca^{2+} impurity (fig. S24). These results indicated that a relatively high density of defects in ASPM perovskite was reduced by the removal of impurities.

Photovoltaic performance and stability

We fabricated p-i-n inverted structure PSCs with the configuration of ITO/2-PACz/$FA_{0.85}MA_{0.1}Cs_{0.05}PbI_3$/$C_{60}$/BCP/Cu { ITO, indium tin oxide; 2-PACz, [2-(9*H*-Carbazol-9-yl) ethyl] phosphonic acid; FA, formamidinium; MA, methylammonium; BCP, bathocuproine} to confirm the performance of ASPM perovskite precursors (Fig. 5A and fig. S25). The PSCs based on the ASPM precursor had a champion efficiency of 25.6%, with an open-circuit voltage (V_{OC}) of 1.19 V, a short-circuit current density (J_{SC}) of 25.0 mA/cm^2, and a fill factor (FF) of 0.860, whereas the control PSCs achieved a champion efficiency of 23.7%, with a V_{OC} of 1.14 V, J_{SC} of 24.9 mA/cm^2, and an FF of 0.832 (Fig. 5B). We compared 40 devices in eight different batches to check the fabrication reproducibility (Fig. 5C). The ASPM devices exhibited good reproducibility, averaging a PCE of 25.0% and a V_{OC} of 1.18 V, whereas the control devices yielded an average PCE of 23.1% and an average V_{OC} of 1.13 V. The ASPM PSCs exhibited a prolonged carrier lifetime [4.29 μs in transient photovoltage (TPV)] and a shorter photocurrent decay [0.326 μs in transient photocurrent (TPC)] compared with those of control PSCs (2.85 μs in TPV and 0.667 μs in TPC), suggesting enhanced radiative recombination and better charge-carrier extraction (fig. S26). The integrated J_{SC} (24.9 mA/cm^2 for ASPM and 24.6 mA/cm^2 for control) from the external quantum efficiency (EQE) matched well with the J_{SC} from the *J-V* curve of 25.0 and 24.9 mA/cm^2 for ASPM and control devices, respectively, within an error of <2% (Fig. 5D and fig. S27). The higher performance of the ASPM devices could be attributed to the removal of the impurities, especially Ca^{2+}, which exerts adverse effects on the performance of PSCs, such as the creation of trap states (fig. S28 and S29).

We tracked the best device for maximum power point (MPP) at 37 ± 1°C with a bias voltage of 1.06 V for 600 s and obtained a steady-state PCE of 25.5% (Fig. 5E), which was higher than the control devices (fig. S30). To further validate our results, we sent one of the best devices based on the ASPM precursor to an accredited independent photovoltaic testing institution and the device achieved a certified PCE of 25.3% (fig. S31) (*35*, *36*). The devices also showed negligible hysteresis (fig. S32 and table S17).

We tested the light stability of the devices under continuous simulated AM1.5G (100 mW/cm^2) light radiation. As shown in Fig. 5F, the unencapsulated PSCs based on ASPM precursor maintained 94% of the original PCE after 1000 hours of light exposure under the N_2 atmosphere, with a surface temperature of 50 ± 5°C. In contrast, the PSCs based on control precursors exhibited a slow decrease within 300 hours, a larger decrease between 300 to 500 hours mainly because of temperature-induced performance degradation and ultimately decreased to 76% of the initial PCE after 1000 hours. Additionally, ASPM devices showed higher stability than control devices even under more extreme thermal and humidity conditions, including under 85°C temperature and 85% relative humidity (fig. S33). The XPS and XRD characterizations proved that the superior stability of ASPM devices was attributed to the high purity of the ASPM perovskite film, which preserved a relatively intact lattice framework, preventing the degradation (fig. S34 and S35).

The ASPM precursor method was also applicable to wide bandgap PSCs. By using a wide bandgap (1.73 eV) composition of $FA_{0.8}Cs_{0.2}Pb(I_{0.7}Br_{0.3})_3$, the ASPM precursor-based PSCs achieved an improvement in PCE from 16.3% to 20.0% in p-i-n structure with an increase in V_{OC} from 1.16 V to 1.27 V (fig. S36).

Discussion

Our study successfully demonstrated the scalable synthesis of ultrapure perovskite microcrystals with an aqueous solution method. We emphasized the detrimental impact of impurities in the perovskite precursor on bulk defects and, consequently, the performance of PSCs. Our findings reveal substantial improvements in both PCE and stability, highlighting the potential of ASPM to address these issues through the elimination of impurities, especially Ca^{2+}. Furthermore, our aqueous synthesis approach proved versatile, enabling the production of various halide- and cation-based lead perovskite microcrystals. This versatility expands the scope of potential applications beyond photovoltaics, offering opportunities for innovation in diverse fields. Therefore, our work not only advances PSC technology but also opens doors to new applications of perovskite materials.

REFERENCES AND NOTES

1. National renewable energy laboratory, best research-cell efficiency chart; www.nrel.gov/pv/cell-efficiency.html.
2. W. Chen *et al*., *Nat. Energy* **7**, 229–237 (2022).
3. Y. Zhang *et al*., *Adv. Mater.* **34**, 2107420 (2022).
4. R. A. Kerner *et al*., *Adv. Mater.* **35**, 2302206 (2023).
5. M. Qin *et al*., *Adv. Mater.* **32**, 2004630 (2020).
6. S. You *et al*., *Science* **379**, 288–294 (2023).
7. H. Zhang, M. K. Nazeeruddin, W. C. H. Choy, *Adv. Mater.* **31**, 1805702 (2019).
8. Z. Ni *et al*., *Science* **367**, 1352–1358 (2020).
9. M. I. Saidaminov *et al*., *Nat. Energy* **3**, 648–654 (2018).
10. R. A. Kerner, K. Schutt, K. Zhu, J. J. Berry, *ACS Energy Lett.* **7**, 4333–4335 (2022).
11. R. A. Kerner *et al*., *ACS Appl. Energy Mater.* **6**, 295–301 (2023).
12. G. S. Shin, Y. Zhang, N. G. Park, *ACS Appl. Mater. Interfaces* **12**, 15167–15174 (2020).
13. A. Wakamiya *et al*., *Chem. Lett.* **43**, 711–713 (2014).
14. M. Ozaki *et al*., *Angew. Chem. Int. Ed.* **58**, 9389–9393 (2019).
15. M. Ozaki *et al*., *J. Mater. Chem. A Mater.* **7**, 16947–16953 (2019).
16. J. Chang *et al*., *J. Mater. Chem. A Mater.* **4**, 887–893 (2016).
17. D. Prochowicz *et al*., *J. Mater. Chem. A Mater.* **3**, 20772–20777 (2015).
18. W. Feng *et al*., *Mater. Today* **50**, 199–223 (2021).
19. J. Park *et al*., *Nature* **616**, 724–730 (2023).
20. D. Wang *et al*., *Adv. Energy Mater.* **13**, 2203649 (2022).
21. Y. Zhang *et al*., *ACS Energy Lett.* **5**, 360–366 (2019).
22. Y. Zhang, S. G. Kim, D. K. Lee, N. G. Park, *ChemSusChem* **11**, 1813–1823 (2018).
23. M. Kim *et al*., *Sustain. Energy Fuels* **4**, 3753–3763 (2020).
24. H. Min *et al*., *Science* **366**, 749–753 (2019).
25. S. Rahimnejad, A. Kovalenko, S. M. Forés, C. Aranda, A. Guerrero, *ChemPhysChem* **17**, 2795–2798 (2016).
26. K. G. Stamplecoskie, J. S. Manser, P. V. Kamat, *Energy Environ. Sci.* **8**, 208–215 (2015).
27. C. C. Stoumpos, C. D. Malliakas, M. G. Kanatzidis, *Inorg. Chem.* **52**, 9019–9038 (2013).
28. L. Wang *et al*., *PLOS ONE* **7**, e51536 (2012).
29. Y. Uchida, T. Sato, *Chem. Senses* **22**, 83–91 (1997).
30. M. Qin *et al*., *Adv. Mater.* **31**, 1901284 (2019).
31. M. Abdelsamie *et al*., *Adv. Funct. Mater.* **30**, 2001752 (2020).
32. N. Mondal, A. Samanta, *Nanoscale* **9**, 1878–1885 (2017).
33. X. Yang *et al*., *Adv. Mater.* **32**, 2002585 (2020).
34. Y. Shao, Z. Xiao, C. Bi, Y. Yuan, J. Huang, *Nat. Commun.* **5**, 5784 (2014).
35. Q. Jiang *et al*., *Nature* **611**, 278–283 (2022).
36. W. Peng *et al*., *Science* **379**, 683–690 (2023).

ACKNOWLEDGMENTS

The authors acknowledge H. Yi at the Southern University of Science and Technology and SUSTech Core Research Facilities for assistance with the characterization of perovskite precursors and films, BL17B1 and BL14B1 beamline of the Shanghai Synchrotron Radiation Facility (SSRF) for the assistance with GIWAXS and in situ GIWAXS measurement, Y. Niu and H. Wang at the Southern University of Science and Technology for assistance with the temperature-dependent capacity test, and Y. Deng at the Southern University of Science and Technology for assistance in the determination of trace water contents.
Funding: The authors acknowledge the support of the National Key Research and Development Project funding from the Ministry of Science and Technology of China (grant no. 2021YFB3800101), the National Natural Science Foundation of China (62204108, 62104094, and U19A2089), the Guangdong Basic and Applied Basic Research Foundation (2021A1515110628, 2023A1515012797, and 2021A1515110606), and Shenzhen Science and Technology Innovation Committee (JCYJ20200109141014474, JCYJ20220530113205013, and JCYJ20220818100211025). N.-G.P. is grateful to the National Research Foundation of Korea grants funded by the Korean government

under contracts NRF-2021R1A3B1076723 (Research Leader Program) and NRF-2022M3J1A1085280 (Carbon Neutral Technology Program).
Author contribution: Y.Z., N.-G.P., X.W., and B.X. supervised the project. Y.Z. conceptualized the research idea and designed the experimental framework. Y.Z. and P.Z. analyzed the experimental data. P.Z. and Y.Z. wrote the manuscript. Y.Z., X.W., N.-G.P., X.W., and B.X. revised the manuscript. P.Z. contributed to synthesizing the perovskite microcrystals and characterizing the perovskite microcrystals and films. P.Z., J.Zh., B.H., Z.L., and X.Z. contributed to characterizing the perovskite films. D.W. contributed to fabricating the inverted perovskite solar cells and performing the stability test. Z.L. contributed to performing the GIWAXS and in situ GIWAXS measurement under the supervision of X.P. L.Z. contributed to analyzing the GIWAXS data. J.L. contributed to the DFT calculation. Y.X. contributed to fabricating the wide-bandgap perovskite solar cells. S.W. contributed to the perovskite microcrystals purity measurement and analysis. J.Ze. and F.H. performed the transient absorption spectroscopy measurement and analysis. All authors contributed to the discussion about the manuscript. **Competing interests:** B.X., P.Z., X.W., and Y.Z., are inventors on patent application CN202211167191.1 submitted by Southern University of Science and Technology that covers the preparation of perovskite microcrystals. The authors declare no other competing interests. **Data and materials availability:** All data are available in the manuscript or the supplementary materials. There are no restrictions on materials sharing. **License information:**

SUPPLEMENTARY MATERIALS

science.org/doi/10.1126/science.adj7081
Materials and Methods
Supplementary Text
Figs. S1 to S36
Tables S1 to S17
References (*37*–*44*)

Submitted 16 July 2023; resubmitted 28 July 2023
Accepted 22 December 2023
10.1126/science.adj7081